

Extraction of sea state from HF radar sea echo: Mathematical theory and modeling

Belinda J. Lipa

Ocean Surface Research, Woodside, California

Donald E. Barrick

Ocean Surface Research, Boulder, Colorado

(Received September 11, 1984; revised April 30, 1985; accepted August 13, 1985.)

We present mathematical methods for the interpretation of high frequency radar sea-echo measured by narrow-beam and CODAR systems. (CODAR is a small transportable radar with a scanning broad beam). These methods are based Barrick's equations for the ocean radar cross section in terms of the directional ocean waveheight spectrum and surface current, using a dimensionless mathematical formulation. In this paper, we describe the simulation of narrow- and broad-beam radar sea-echo from both deep and shallow water, discussing the effect of ocean surface currents, including vertical and horizontal current shear. This paper provides the mathematical tools for the modeling of common experimental situations in HF radar oceanography; such models are used in subsequent papers that describe the extraction of sea-state information from HF radar sea-echo data.

1. INTRODUCTION

The potential of high frequency (HF) radar devices for the remote monitoring of sea-surface parameters has been recognized since *Crombie* [1955] observed and identified the distinctive features of sea-echo Doppler spectra. Rapid advances in the implementation of quantitative measurement techniques ensued after the derivation by *Barrick* [1972a, b] of the exact theoretical formulation that expresses the HF sea-echo Doppler spectrum in terms of the ocean waveheight directional spectrum and the surface current velocity. Interpretation and inversion of these theoretical relationships allows ocean surface parameters to be derived from observed data without resort to the empirical models required, for example, for the interpretation of microwave scatterometer measurements [*Barrick and Swift*, 1980].

On the basis of antenna beamwidth, two types of HF radar systems may be identified. The first comprises narrow-beam systems, which were developed initially for the over-the-horizon detection and tracking of military targets. Narrow-beam systems have been employed both in groundwave and skywave modes for the remote observation of sea-surface properties [*Lipa et al.*, 1981]. Although the interpre-

tation of the narrow-beam signal backscattered from the sea is simpler, the disadvantage of narrow-beam systems for most applications is their huge physical size, and consequent high installation and operating cost. It is mainly for this reason that the second class was developed: small transportable systems with broad beams that rely on novel antenna concepts to provide adequate angular resolution of sea-surface features. These systems are termed CODAR (for Coastal Ocean Dynamics Applications Radar). Original CODAR concepts were developed in NOAA's Wave Propagation Laboratory for the measurement of surface currents; these research investigations employed a separate transmit antenna along with 3- and 4-element monopole arrays for receive [*Barrick et al.*, 1977]. In later efforts to extend CODAR to measure coastal directional wavefields and overcome technical difficulties with the 4-element array, an even more compact antenna system was developed [*Barrick and Lipa*, 1979], consisting of three elements: two crossed loops and a monopole, now used for both transmit and receive. This system is about 2 m high and 0.6 m wide; it measures both the ocean waveheight directional spectrum [*Lipa and Barrick*, 1982b] and the surface-current field [*Lipa and Barrick*, 1983], from the coast and from offshore platforms. This is now the only CODAR antenna system in use within the USA, although the older CODAR antenna system is still operated in Canada and West Germany.

Copyright 1986 by the American Geophysical Union.

Paper number 5S0655.
0048-6604/86/005S-0655\$08.00

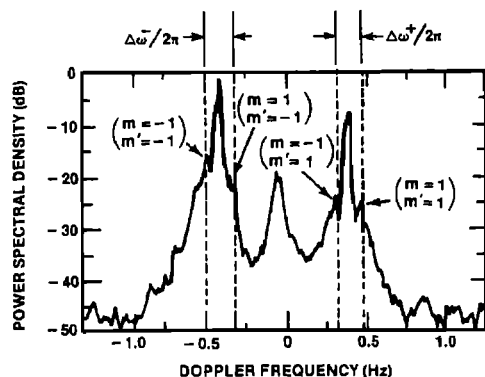


Fig. 1. An 84-sample sea echo power spectrum recorded by the SRI skywave radar on May 17, 1978, 1628 UT at 15 MHz. The first-order Bragg peaks occur at ± 0.395 Hz. The dashed lines indicate the positions of the four second-order peaks produced by a 12-s swell.

In previous publications, we have demonstrated the validity of narrow- and broad-beam HF radar measurements for directional waveheight spectral measurements [Lipa *et al.*, 1981; Lipa and Barrick, 1982b]. Analytical and computational techniques for the modeling and inversion of narrow-beam HF radar sea-echo have been described in report form by Lipa and Barrick [1982a]. However we have not yet presented details of the methods which are implemented as automatic, operational software for CODAR measurement of the directional spectrum, as we have done for surface currents [Lipa and Barrick, 1983]. The mathematics required for the interpretation and inversion of the second-order radar spectrum to give sea-state is far more complicated than that for currents. It is the purpose of this and subsequent papers to present and demonstrate these methods.

The measurement of the statistical waveheight spectrum with any instrument requires averaging over time and/or area. The accuracy obtainable for a given resolution depends on the measurement technique; for HF radar, waveheight directional spectra can typically be obtained every $\frac{1}{2}$ hour over areas as small as 25 square kilometers. Due to the properties of the second-order integral, the frequency resolution of the derived wave spectrum decreases with wave period; this sets a lower limit of about 3.5 sec on the period of the recovered information. Within the radar scattering region, the directional spectrum must either be homogeneous or able to be mathematically modeled. Because of these restrictions, HF radar wave measurements are made with fairly

simple configurations: for example from an island or platform in the open ocean or from a simple coastline with a clear ocean view. This excludes from consideration operation in rivers, straits, estuaries and any constrained areas with highly inhomogeneous or unstable conditions. (These constraints do not apply to CODAR measurements of surface currents, which have been made in many such areas). Also excluded is the surf zone close to the beach due to the highly nonlinear wave dynamics; in any case, that region is automatically excluded from HF radar measurements by receiver shutdown to allow the transmit pulse to escape the area.

2. NARROW-BEAM RADAR SEA ECHO

Figure 1 shows a typical, measured HF Doppler spectrum of radar echo backscattered near grazing incidence from the sea at 15 MHz. The dominant contribution is produced by first-order scatter from specific spectral components of the ocean wavefield. These surface-height spectral components are termed "Bragg waves"; their wavelength is exactly one-half the radar wavelength, and they move directly toward or away from the radar station. These peaks are evident in Figure 1; their amplitude is two orders of magnitude higher than the surrounding continuum, from which they are separated by well-defined nulls. In the absence of ocean current, the first-order peaks occur at frequencies that depend only on the radar transmitter frequency. The surrounding continuum is due to higher-order scatter, the greater part of which arises from second-order interaction between pairs of ocean waves constituting the total ocean wavefield. It is from the interpretation of this portion of the spectrum (normalized by the first-order energy) that we derive the directional ocean waveheight spectrum. The random appearance of the radar spectrum is due to the random height of the wavetrains composing the surface of the sea. The scatter of the resulting spectral points is described by a χ^2 (chi-squared) distribution with $2N$ degrees of freedom, where N is the number of spectra averaged [Barrick and Snider, 1977].

The Doppler spectrum can be expressed as the radar cross section per mean surface area per rad/s. bandwidth $\sigma(\omega, \phi)$, which is a function of the Doppler frequency shift ω from the carrier and the bearing angle ϕ of the radar beam with respect to an arbitrary fixed direction.

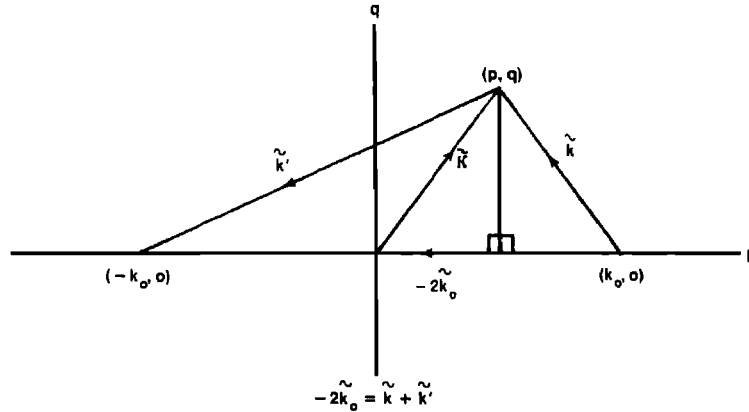


Fig. 2. Illustration of the second-order interaction process. The incident radar wave (wavevector \tilde{k}_0) interacts with the first ocean wavetrain (\tilde{k}) to produce an intermediate scattered wave (\tilde{k}). This interacts with a second wavetrain (\tilde{k}') to produce a wave which is scattered back towards the radar. Integration point (p, q) of the second-order integral is at the intersection of the wavevectors $\tilde{k}, \tilde{k}, \tilde{k}'$. The perpendicular from (p, q) to the p -axis is useful for proving many of the equations in the text.

2.1. The narrow-beam deep-water radar cross section

Barrick's [1972a] equation for the first-order radar spectral cross section in deep water in the absence of ocean of surface current is given by

$$\sigma^{(1)}(\omega, \phi) = 2^6 \pi k_0^4 \sum_{m' = \pm 1} S(-2m'\tilde{k}_0) \delta(\omega - m'\omega_B) \quad (1)$$

where $m' = \pm 1$ denotes the sign of the Doppler shift, \tilde{k}_0 is the radar wave vector (of magnitude k_0 pointing toward the scattering patch), and $S(\)$ is the directional waveheight spectrum. The Bragg resonance condition is imposed by the delta-function constraint. Thus, ideally, the first-order peaks are impulse functions at the Bragg frequencies $\pm\omega_B$, defined in terms of the radar wavenumber k_0 for deep water by the dispersion equation

$$\omega_B = \sqrt{2gk_0} \quad (2)$$

where g is the gravitational acceleration.

In practice, these peaks are broadened somewhat by current turbulence, ionospheric motions (in a sky-wave radar), and systems effects. The amplitudes of the first-order peaks are proportional to the directional ocean-wave spectrum at the Bragg wave vectors $\pm 2\tilde{k}_0$. At normal HF frequencies, these correspond to short, saturated waves (e.g., 2-s period for a radar frequency of 25 MHz).

Barrick's equation (1972b) for the second-order radar spectral cross section at a Doppler shift ω is given by

$$\sigma^{(2)}(\omega, \phi) = 2^6 \pi k_0^4 \sum_{m, m' = \pm 1} \int_{-\infty}^{\infty} \int_{-\infty}^{\infty} |\Gamma|^2 S(m\tilde{k}) S(m'\tilde{k}') \delta(\omega - m\sqrt{gk} - m'\sqrt{gk'}) dp dq \quad (3)$$

Here, the spatial wavenumber p is defined to lie along the radar beam, with q perpendicular. In the second-order scattering process, a first set of waves of wavevector \tilde{k} interacts with the incident radar wave (\tilde{k}_0) to produce a scattered wave \tilde{k} (Figure 2). A second interaction with waves of wavevector \tilde{k}' takes the incident intermediate wave and scatters it back toward the radar. The scattering wave vectors \tilde{k} and \tilde{k}' are defined by

$$\tilde{k} = (p - k_0, q) \quad \tilde{k}' = (-(p + k_0), -q) \quad (4)$$

and hence they obey the constraint

$$\tilde{k} + \tilde{k}' = -2\tilde{k}_0 \quad (5)$$

The lengths of the scattering wave vectors are denoted by k and k' . The values of m and m' in (3) take the values $+1$ and -1 , defining the four possible combinations of direction of the two scattering waves. The coupling coefficient Γ is given by

$$\Gamma = \Gamma_H + \Gamma_{EM} \quad (6)$$

where Γ_H and Γ_{EM} are the hydrodynamic and electromagnetic components defined by

$$\Gamma_H = \frac{-i}{2} \left[k + k' - \frac{(kk' - \tilde{k} \cdot \tilde{k}')(\omega^2 + \omega_B^2)}{mm' \sqrt{kk'}(\omega^2 - \omega_B^2)} \right] \quad (7)$$

$$\Gamma_{EM} = \frac{1}{2} \left[\frac{(\tilde{k} \cdot \tilde{k}_0)(\tilde{k}' \cdot \tilde{k}_0)/k_0^2 - 2\tilde{k} \cdot \tilde{k}'}{\sqrt{k \cdot k'} - k_0 \Delta} \right] \quad (8)$$

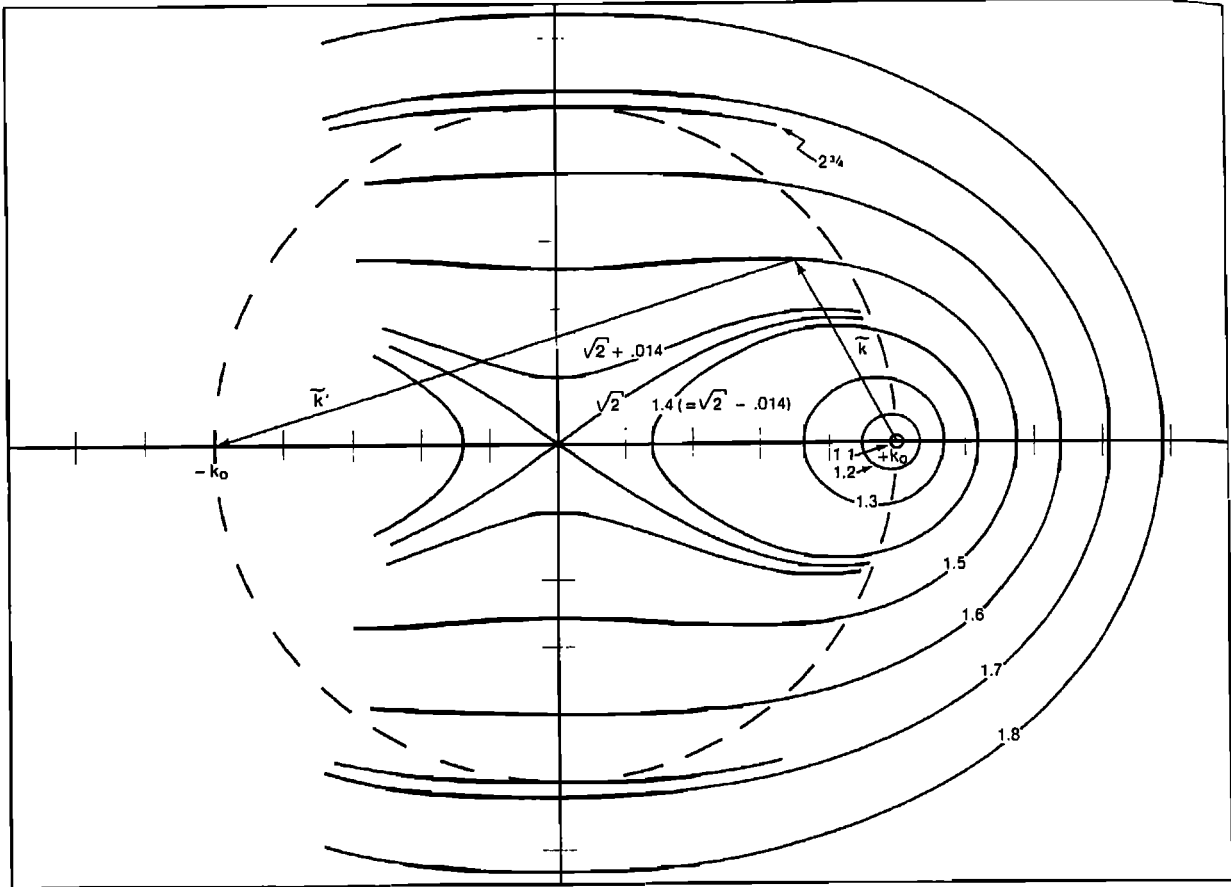


Fig. 3. Normalized constant Doppler frequency contours, η , vs. wavenumbers, k and k' , for the two ocean wave vectors \vec{k} and \vec{k}' producing second-order backscatter, for $|\omega| > \omega_p$ (i.e., $m = m'$). Shown is the mathematically singular situation at $|\eta| = \sqrt{2}$, where the two closed contours break apart. The dashed circle shows the electromagnetic "corner reflector" condition, where \vec{k} and \vec{k}' are at right angles ($\vec{k} \cdot \vec{k}' = 0$); this circle is tangent to the Doppler frequency contour $|\eta| = 2^{3/4}$, producing a mathematical stationarity or peak at this frequency. The contours are symmetric about the q axis.

The derivation of these coupling coefficients is discussed in Appendix A. Equation (3) for the second-order radar spectrum is a perturbation solution of the nonlinear hydrodynamic and electromagnetic boundary conditions at the ocean surface to second order in both waveslope and the perturbation parameter $k_0 h$, where h is the rms waveheight. For this solution to be applicable, the perturbation parameter must be less than unity, which sets the following approximate limit on the waveheight for a given radar wavenumber:

$$h < 1/k_0 \quad (9)$$

If the sea-state exceeds this limit, the second-order radar spectrum begins to saturate, and the value of the ocean waveheight predicted through interpreta-

tion of (3) will be too low; in this case a lower transmit frequency should be used.

Frequency contours are defined by the delta function constraints in (3). They are the loci of the points (p, q) in Figure 2 giving the lengths and directions of the two interacting wave vectors, \vec{k} and \vec{k}' , that contribute to second-order scatter at a given, constant Doppler frequency. We will now prove that the different combinations of m and m' define disjoint ranges of Doppler frequency.

2.1.1. *The case $m = m'$.* Squaring the argument of the delta function in (3) gives the relation

$$\omega^2 = g(k + k' + 2\sqrt{kk'}) \quad (10)$$

where k and k' are the lengths of the scattering wave vectors. It follows from Figure 2 that because the

sum of two sides of a triangle is always greater than the third we have

$$k + k' > 2k_0 \quad (11)$$

Since $(kk')^{1/2}$ is positive, it follows from (10) and (11) that

$$\omega^2 > 2gk_0 \quad (12)$$

This therefore defines the regions of Doppler frequency outside the Bragg lines; i.e.,

$$\omega > \sqrt{2gk_0} \quad m = m' = +1 \quad (13)$$

$$\omega \leq \sqrt{2gk_0} \quad m = m' = -1 \quad (14)$$

The frequency contours are plotted in Figure 3. The Bragg frequencies $\pm\omega_B$ define the points $(p, q) = (\pm k_0, 0)$ where one of the two interacting ocean wavenumbers is zero (i.e., infinite wavelength). Such ocean waves do not exist, and the corresponding directional spectral value in (3) will be zero, together with the value of the second-order radar cross section. This is the reason for the nulls between the first and second-order spectra that can be seen in Figure 1. Close to the Bragg frequency, the frequency contours are almost circular in shape, and have a radius much smaller than the radar wavenumber k_0 . Therefore both of the scattering wave vectors \vec{k} and \vec{k}' are almost constant in length around the frequency contour with the longer approximately equal in length to $2k_0$. The eccentricity of the contours increases with departure from the Bragg frequency until a caustic occurs when $|\omega| = \sqrt{2}\omega_B$. This gives rise to singularities in the radar spectrum at these frequencies.

2.1.2. *The case $m \neq m'$.* Squaring the argument of the delta function now gives

$$\omega^2 = g(k + k' - 2\sqrt{kk'}) \quad (15)$$

If we consider first the half plane of (p, q) space for which $k < k'$, then leads to the inequality

$$\omega^2 < g(k' - k) \quad (16)$$

It can be seen from Figure 2 that the maximum value of $(k' - k)$ equals $2k_0$ and occurs when the vectors lie in opposite directions along the p axis. Therefore from (16)

$$\omega^2 < 2gk_0 \quad (17)$$

which defines the region between the Bragg lines:

$$\begin{aligned} 0 < \omega \leq \omega_B & \quad m = 1, m' = -1 \\ -\omega_B < \omega \leq 0 & \quad m = -1, m' = 1 \end{aligned} \quad (18)$$

A similar proof applies to the left-half plane with the results

$$\begin{aligned} 0 < \omega \leq \omega_B & \quad m = -1, m' = 1 \\ -\omega_B < \omega \leq 0 & \quad m = 1, m' = -1 \end{aligned} \quad (19)$$

Frequency contours are shown in Figure 4. As for the case $m = m'$, they are almost circular close to the Bragg frequency but in this case change shape in a regular fashion with increasing frequency displacement from the Bragg line.

2.1.3. *Calculation of the deep-water radar cross section.* We now describe how to calculate values for the second-order radar cross section for a model of the ocean directional waveheight spectrum. It is convenient to transform (1) and (3) to a dimensionless form, which is achieved by expressing the product $\omega_B \sigma^{(2)}(\omega)$ as a function of the normalized variables $k/2k_0$ and ω/ω_B . Results for any calculation then apply to a family of ocean spectral models and radar frequencies having the same values of the normalized parameters. The delta-function constraint is used to perform one of the integrations in (3); the other must generally be performed numerically.

Any model for the ocean-wave spectrum may be used; we choose as an example the product of a Pierson-Moskowitz nondirectional spectrum [Moskowitz, 1964] and a cardioid directional factor. The wave vector \vec{k} defined in (4) may be written in polar coordinates as $(k, \theta + \phi)$, where θ is the angle with respect to the radar beam and ϕ is the angle between the radar beam and the fixed reference direction. The model ocean wave spectrum is defined by

$$S(\vec{k}) = f(k)g(\theta + \phi) \quad (20)$$

where the Pierson-Moskowitz spectrum $f(k)$ describes the characteristic falloff of saturated waves above a cutoff region defined by wavenumber k_c :

$$f(k) = \frac{0.005e^{-0.74(k_c/k)^2}}{k^4} \quad (21)$$

and we express the directional factor as a Fourier series over angle:

$$g(\alpha) = \frac{1}{2\pi} \sum_{n=-2}^2 c_n t_f^n(\alpha) \quad (22)$$

in which c_n are Fourier angular coefficients and $t_f^n(\alpha)$ are trigonometric functions defined by

$$\begin{aligned} t_f^n(\alpha) &= \cos(n\alpha) & n \geq 0 \\ &= \sin(-n\alpha) & n < 0 \end{aligned} \quad (23)$$

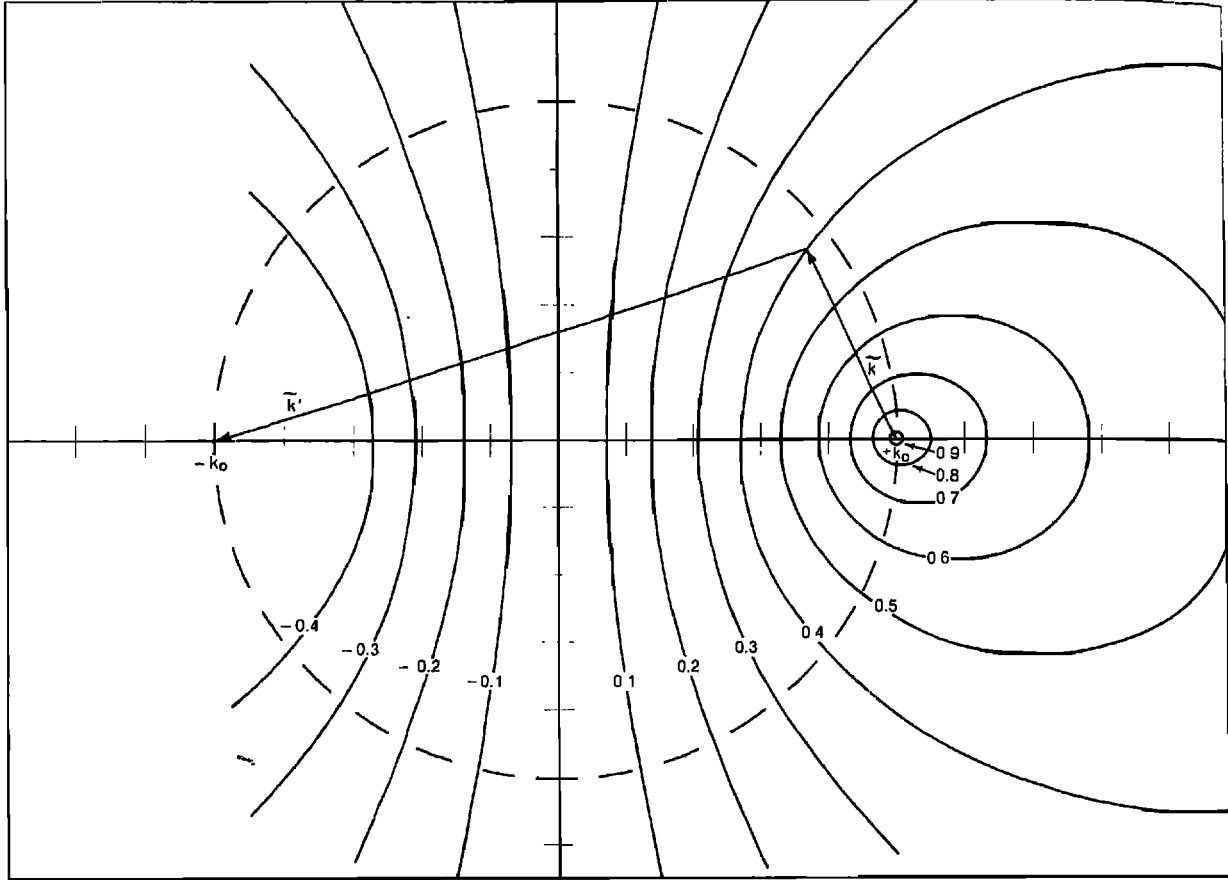


Fig. 4. Normalized constant Doppler frequency contours, η , vs. wavenumbers k and k' , for the two ocean wave vectors \vec{k} and \vec{k}' producing second-order backscatter, for $|\omega| < \omega_B$ (i.e., $m = -m'$). The dashed circle representing the electromagnetic "corner-reflector" condition is not tangent to any Doppler frequency contour; therefore there are no peaks due to this phenomenon between the Bragg lines. The contours are symmetric about the q axis.

The Fourier series can represent a wide range of directional distributions; for example we consider a cardioid distribution given by

$$g(\alpha) = \cos^4\left(\frac{\alpha - \alpha^*}{2}\right) / \int_{-\pi}^{\pi} \cos^4\left(\frac{\alpha}{2}\right) d\alpha \quad (24)$$

it has Fourier coefficients defined by

$$\begin{aligned} c_{-2} &= \sin(2\alpha^*)/3 \\ c_{-1} &= 4 \sin(\alpha^*)/3 \\ c_0 &= 1 \\ c_1 &= 4 \cos(\alpha^*)/3 \\ c_2 &= \cos(2\alpha^*)/3 \end{aligned} \quad (25)$$

The wave spectrum is normalized so that the integral over k is equal to the mean-square waveheight h^2 ; i.e.,

$$h^2 = \int_0^{\infty} \int_{-\pi}^{\pi} S(\vec{k}) k dk d\theta \quad (26)$$

We define the following normalized variables:

Wave vector

$$\vec{K} = \vec{k}/2k_0 \quad \vec{K}' = \vec{k}'/2k_0 \quad (27)$$

Wavenumber

$$K = |\vec{K}| \quad K' = |\vec{K}'| \quad (28)$$

Frequency

$$\eta = \omega/\omega_B \quad (29)$$

RMS waveheight

$$H = 2k_0 h \quad (30)$$

Coupling coefficient

$$\gamma_H = \frac{\Gamma_H}{2k_0} \quad \gamma_{EM} = \frac{\Gamma_{EM}}{2k_0} \quad \gamma_L = \gamma_H + \gamma_{EM} \quad (31)$$

Nondirectional spectrum

$$F(K) = (2k_0)^4 f(k) \quad (32)$$

Ocean-wave directional spectrum

$$Z(\vec{K}) = (2k_0)^4 S(\vec{k}) \quad K_c = k_c/2k_0 \quad (33)$$

Note that with these definitions, the integral over $Z(\vec{K})$ is equal to the normalized mean-square wave-height H^2 . It is also convenient to define through the following equations two new parameters: a dimensionless variable u , which is the magnitude of the normalized frequency shift from the Bragg line,

$$u = m(\eta - m') \quad (34)$$

and a parameter L , which is $+1$ outside the Bragg lines (where $m = m'$) and -1 within (where $m \neq m'$):

$$L = mm' \quad (35)$$

The indices m, m' define the four second-order regions of the Doppler spectrum: (1) $m = m' = +1$ corresponds to $\eta > 1$ or $\omega > \omega_B$; (2) $m = -1, m' = +1$ corresponds to $0 < \eta < 1$ or $0 < \omega < \omega_B$; (3) $m = +1, m' = -1$ corresponds to $-1 < \eta < 0$ or $-\omega_B < \omega < 0$; (4) $m = m' = -1$ corresponds to $\eta < -1$ or $\omega < -\omega_B$. From the definitions (7) and (8) for Γ_H and Γ_{EM} the normalized coupling coefficients can be written as

$$\gamma_H = \frac{-i}{2} \left[K + K' - \frac{(KK' - \vec{K} \cdot \vec{K}')(\eta^2 + 1)}{L\sqrt{KK'}(\eta^2 - 1)} \right] \quad (36)$$

$$\gamma_{EM} = \frac{1}{2} \left[\frac{(\vec{K} \cdot \hat{k}_0)(\vec{K}' \cdot \hat{k}_0) - 2\vec{K} \cdot \vec{K}'}{\sqrt{\vec{K} \cdot \vec{K}' - \Delta/2}} \right] \quad (37)$$

where \hat{k}_0 is the unit vector pointing from the radar to the scattering patch. In terms of the dimensionless variables, the delta-function constraint becomes

$$\delta(\omega - m'\sqrt{gk'} - m\sqrt{gk}) = \delta(\eta - m'\sqrt{K'} - m\sqrt{K})/\omega_B \quad (38)$$

By symmetry, the values of the integral in (3) taken over the right and left half planes are identical; we will therefore take the integral only over the right half plane (where $K < K'$) and double the result. We use as integration variables the polar coordinates K, θ of the shorter scattering wave vector; it can be shown from Figure 2 that in terms of these variables the coordinates of the longer wave vector are

$$K' = \sqrt{K^2 + 2K \cos \theta + 1} \quad (39)$$

$$\theta' = \sin^{-1}(K \sin \theta / K') + \pi \quad (40)$$

We can now redefine the first- and second-order radar cross sections (1) and (3) in the following dimensionless form, using equations (27) to (40)

$$\sigma_1(\eta, \phi) \equiv \omega_B \sigma^{(1)}(\omega) = 4\pi \sum_{m'=\pm 1} Z(-m'\hat{k}_0)\delta(\eta - m') \quad (41)$$

$$\sigma_2(\eta, \phi) \equiv \omega_B \sigma^{(2)}(\omega)$$

$$= 8\pi \sum_{m,m'=\pm 1} \int_0^\infty \int_{-\pi}^\pi |\gamma_L|^2 \delta(\eta - m\sqrt{K} - m'\sqrt{K'}) \cdot Z(m\vec{K})Z(m'\vec{K}')K dK d\theta \quad (42)$$

One of the integrations in (42) is easily performed using the delta function constraint on the variables. The form of (42) suggests the definition of new variables as follows:

$$y = \sqrt{K} \quad (43)$$

$$h(y, \theta) = my + m'\sqrt{K'} \quad (44)$$

$$I(y, \theta) = 2^4 \pi |\gamma_L|^2 Z(m\vec{K})Z(m'\vec{K}')y^3 \quad (45)$$

Substituting these definitions in (42) gives the following simple form:

$$\begin{aligned} \sigma_2(\eta, \phi) &= \iint I(y, \theta) \delta(\eta - h(y, \theta)) dy d\theta \\ &= \iint I(y, \theta) \delta(\eta - h(y, \theta)) \left| \frac{\partial y}{\partial h} \right|_0 dh d\theta \end{aligned} \quad (46)$$

where the factor $|\partial y / \partial h|_0$ can be obtained by differentiating (44).

$$\left| \frac{\partial y}{\partial h} \right|_0 = \frac{1}{|1 + Ly(y^2 + \cos \theta)/(1 + 2y^2 \cos \theta + y^4)^{3/4}|} \quad (47)$$

This factor has an integrable singularity at the origin where $\theta = \pi$ and $y = 1/\sqrt{2}$, and at $|\eta| = \sqrt{2}$ (see Figure 3).

The equation

$$\eta - h(y^*, \theta) = 0 \quad (48)$$

is solved numerically using a Newton-Raphson method to give y^* as a function of θ . The integral (46) then reduces to

$$\sigma_2(\eta, \phi) = \int_{-\theta_L}^{\theta_L} I(y^*, \theta) \left| \frac{\partial y}{\partial h} \right|_{y=y^*} d\theta \quad (49)$$

where θ_L defines the limiting angle.

It can be seen from Figure 3 and 4 that for integration over the right-half plane, the value of θ defined by a frequency contour usually ranges from $-\pi$ to π . However for $\eta^2 > 2$, the contour intersects the q axis, and the limits on θ must be obtained by solving for

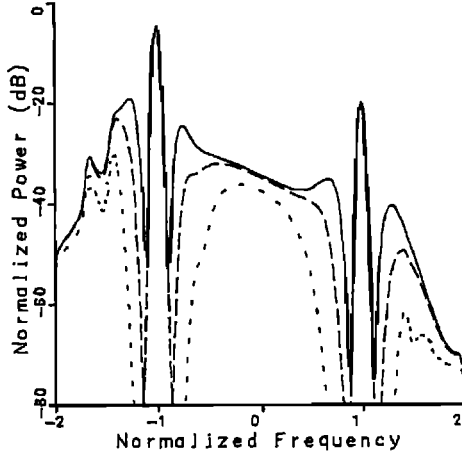


Fig. 5. Simulated spectra showing the effect of increasing waveheight on the normalized Doppler radar spectrum, using the cardioid model defined by (24) for the directional distribution and the Pierson-Moskowitz nondirectional spectrum defined by (21). Ocean-wave direction is 45° with respect to the radar beam; normalized waveheight; 1.87 (continuous line), 0.66 (long-dashed), 0.17 (short-dashed). This corresponds to normalized cutoff wavenumbers of 0.1, 0.2, 0.5. The whole spectrum is smeared in normalized frequency using a Gaussian window of width 0.05.

the points of intersection. It follows from Figure 2 that at the q axis, where K and K' are equal, the limiting values θ_L are given by

$$\theta_L = \pm[\pi - \cos^{-1}(2/\eta^2)] \quad \eta^2 > 2 \quad (50)$$

The integration in (49) must be performed numerically as a closed form solution does not exist in general. We used the trapezoidal rule except in the immediate vicinity of a singularity in the electromagnetic coupling coefficient, which occurs when the scalar product $\vec{K} \cdot \vec{K}'$ in the denominator of (37) becomes zero. The condition $\vec{K} \cdot \vec{K}' = 0$ defines a circle in the (p, q) plane which is shown in Figures 3 and 4, marking the transition between propagating and evanescent intermediate radio waves scattered between the two ocean wave trains. To allow for the effect of the singularity, we integrated separately over the segment of frequency contour bounded by the two circles defined by

$$K \cdot K' = \pm 0.01 \quad (51)$$

Over this segment a variable transformation was used so that the distance between quadrature points decreases exponentially as the singular circle is approached.

The electromagnetic singularity causes a peak in the radar cross section at a value of normalized fre-

quency equal to $2^{3/4}$, where the frequency contour is tangential to the circle of singularity. Away from this region, the radar cross section is insensitive to the precise value of the normalized surface impedance Δ and, as discussed in Appendix A, we have found it adequate to use an average value given by

$$\Delta = 0.011 - i(0.012) \quad (52)$$

Figures 5 and 6 give examples of simulated spectra calculated from (41) and (42). To simulate the finite frequency resolution of a practical system, we have smeared the theoretical Doppler spectrum in normalized frequency using a Gaussian window of normalized width 0.05. Figure 5 illustrates the effect of changing waveheight; the Doppler spectrum is shown for three different values of waveheight at the same dominant ocean-wave direction (45° with respect to the radar beam). For the ocean-wave spectral model used, increasing waveheight is equivalent to increasing the peak waveperiod. The resulting amplitude of the second-order spectrum increases relative to the first, and the spectral peak moves closer to the Bragg line. Figure 6 illustrates the effect of changing the dominant wave direction at constant waveheight; the Doppler spectrum is shown for three values of dominant wave direction, α^* , relative to the radar beam (0° , 45° , 90°). The degree of symmetry about zero Doppler increases as the wave direction tends to perpendicular.

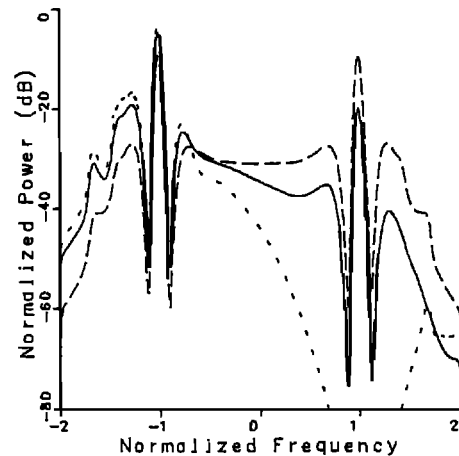


Fig. 6. Simulated spectra showing the effect of changing ocean-wave direction. The ocean-wave spectral model and the frequency smearing are the same as for Figure 5, the normalized cutoff wavenumber is 0.1, the dominant ocean-wave directions with respect to the radar beam are 90° (long-dashed), 45° (continuous), 0° (short-dashed).

2.2. The narrow-beam shallow-water radar cross section

The analysis of the preceding section must be revised in shallow water to allow for modifications in the coupling coefficients, the dispersion equation and the directional spectrum. We only consider water of sufficient depth, however, that the effects of wave energy dissipation such as breaking may be ignored; as a general rule, this assumption is valid when the water depth is greater than 1/20 the deep-water wavelength.

The equations for the backscattered signal Doppler spectrum (1) and (3) must first be altered to account for the lowest-order shallow-water dispersion relation. To first-order in scatter, we have the following spatial and temporal wavenumbers:

$$\begin{aligned} \vec{k}'_s &= -2\vec{k}_0 \\ \omega'_s &= m'\omega_B = m'\sqrt{2gk_0 \tanh(2k_0 d)} \end{aligned} \quad (53)$$

where d is the water depth and k'_s , ω'_s are the spatial, temporal wavenumbers of the first-order ocean wave component producing the backscatter. The analogous relationships for second-order backscatter are

$$\begin{aligned} \vec{k}_s + \vec{k}'_s &= -2\vec{k}_0 \\ m\sqrt{gk_s \tanh(k_s d)} + m'\sqrt{gk'_s \tanh(k'_s d)} &= \omega \end{aligned} \quad (54)$$

where here \vec{k}_s and \vec{k}'_s are the spatial wavevectors of the two shallow-water, first-order ocean waves interacting to produce second-order backscatter.

The electromagnetic coupling coefficient in (3) has the same form as in (8), with the shallow-water wavevectors used in place of the deep-water ones:

$$\Gamma_{EM}^{\pm} = \frac{1}{2} \left[\frac{(\vec{k}_s \cdot \vec{k}_0)(\vec{k}'_s \cdot \vec{k}_0)/k_0^2 - 2\vec{k}_s \cdot \vec{k}'_s}{\sqrt{\vec{k}_s \cdot \vec{k}'_s - k_0 \Delta}} \right] \quad (55)$$

However, the hydrodynamic coupling coefficient, derived by *Barrick and Lipa* [1986] through solution of the equations of motion and continuity, is a function of water depth given by

$$\begin{aligned} \Gamma_H^{\pm} &= \frac{-i}{2} \left\{ k + k' - \frac{(kk' - \vec{k}_s \cdot \vec{k}'_s)}{mm' \sqrt{kk'}} \left(\frac{\omega^2 + \omega_B^2}{\omega^2 - \omega_B^2} \right) \right. \\ &\quad \left. + \frac{\omega[(m\sqrt{gk})^3 \operatorname{csch}^2(k_s d) + (m'\sqrt{gk'_s})^3 \operatorname{csch}^2(k'_s d)]}{g(\omega^2 - \omega_B^2)} \right\} \end{aligned} \quad (56)$$

where the equivalent deep- and shallow-water spatial wavenumbers have the following relationship:

$$k = k_s \tanh(k_s d) \quad k' = k'_s \tanh(k'_s d)$$

In normalized form we have

$$\begin{aligned} \gamma_H^{\pm} = \Gamma_H^{\pm}/2k_0 &= \frac{-i}{2} \left\{ K + K' + L \frac{(KK' - \vec{K}_s \cdot \vec{K}'_s)}{\sqrt{KK'}} \left(\frac{1 + \eta^2}{1 - \eta^2} \right) \right. \\ &\quad \left. - \frac{(\sqrt{K} + L\sqrt{K'})(K^{3/2} \operatorname{csch}^2(K_s D) + LK'^{3/2} \operatorname{csch}^2(K'_s D))}{\tanh D(1 - \eta^2)} \right\} \end{aligned} \quad (57)$$

where the normalized depth is defined by

$$D \equiv 2k_0 d \quad (58)$$

As illustrated in Figure 7, the hydrodynamic coupling coefficient increases as the water depth decreases (at constant wavenumber, K_s , of the dominant wave component), and also with decreasing wavenumber at constant depth. This can also be seen from the asymptotic limit as $\vec{K} \cdot D \rightarrow 0$, when (57) has the simple form

$$\gamma_H = i \left[\frac{\cos \theta_s}{\tanh(K_s D)} \right] \quad (59)$$

where θ_s is the angle between the radar beam and the shallow-water ocean wave. This behavior can be understood physically as follows: if one considers a solitary, periodic (Stokes) wave, then Γ_H^{\pm} represents the second-harmonic spatial correction to its height profile, which to lowest order is a sinusoid. This second spatial harmonic, as it increases, causes the crests to steepen and the troughs to become flatter, until instability causes the wave to break, dissipating its energy. This is a phenomenon which can be observed at a

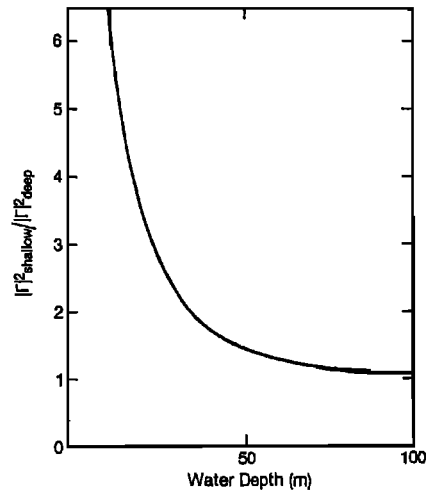


Fig. 7. The ratio of the hydrodynamic coupling coefficient in shallow water to that in deep water for a 16-s ocean wave parallel to the radar beam, radar frequency 25.4 MHz.

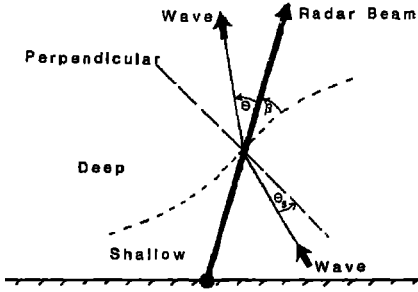


Fig. 8. Schematic geometry of the radar beam and an ocean wave train at a depth discontinuity, denoted by the dashed line.

beach when waves rise up and break as they come into very shallow water from a seemingly calm sea in the distance.

In the following analysis, it is assumed that all inhomogeneity in the directional wave spectrum arises from wave refraction in shallow water; i.e. the corresponding directional spectrum in deep water is homogeneous. It follows from linear wave theory that since the total energy in the wavefield (neglecting energy dissipation) must be conserved, the shallow-water wave spectrum expressed in the appropriate variables has exactly the same value as the deep-water spectrum [Kinsman, 1965]

$$S_s(\vec{k}_s) = S(\vec{k}) \quad (60)$$

where the transformation between shallow- and deep-water wave vectors comes from Snell's law and the dispersion equation:

$$k \cos(\theta + \beta) = k_s \cos(\theta_s + \beta) \quad (61)$$

$$k = k_s \tanh(k_s d) \quad (62)$$

with β the angle between the radar beam and the depth contour, and θ_s , θ the angles between the radar beam and the shallow, deep water ocean waves, respectively (see Figure 8). The normalized equations for the first- and second-order radar cross sections in shallow water are given by

$$\sigma_1^2(\eta, \phi, D, \beta) = 4\pi \sum_{m'=\pm 1} Z_s(-m'\vec{k}_0)\delta(\eta - m') \quad (63)$$

$$\begin{aligned} \sigma_2^2(\eta, \phi, D, \beta) = & 8\pi \sum_{m,m'=\pm 1} \\ & \int_0^\infty \int_{-\pi}^\pi |\gamma_L|^2 Z_s(m\vec{K}_s)Z_s(m'\vec{K}'_s)\delta(\eta - m\sqrt{K_s \tanh(K_s D)} \\ & - m'\sqrt{K'_s \tanh(K'_s D)})K_s dK_s d\theta_s \end{aligned} \quad (64)$$

where the wavenumbers of the scattering waves are related through (54):

$$K'_s = (K_s^2 + 2K_s \cos \theta_s + 1)^{1/4} \quad (65)$$

To compute the second-order integral in (64) we choose as integration variables $y_s = \sqrt{K_s}$ and the deep water angle θ . In terms of these variables (64) becomes:

$$\sigma_2^2(\eta, \phi, D, \beta) = \iint I(y_s, \theta)\delta(\eta - h(y_s, \theta)) \left| \frac{\partial y_s}{\partial h} \right| dh d\theta \quad (66)$$

where

$$h(y_s, \theta) = m y_s \sqrt{\tanh(y_s^2 D)} + m' \sqrt{K'_s} \quad (67)$$

$$I(y_s, \theta) = 2^4 \pi |\gamma_L|^2 Z(m\vec{K})Z(m'\vec{K}')y_s^3 \left(\frac{\partial \theta_s}{\partial \theta} \right)_y \quad (68)$$

The factors $(\partial \theta_s / \partial \theta)_y$ and $|\partial y_s / \partial h|_\theta$ are obtained by differentiating (61) and (67)

$$(\partial \theta_s / \partial \theta)_y = \tanh(y_s^2 d) \frac{\sin(\theta + \beta)}{\sin(\theta_s + \beta)} \quad (69)$$

$$\begin{aligned} \left| \frac{\partial y_s}{\partial h} \right|_\theta = & \left[\sqrt{\tanh(y_s^2 d)} + \frac{y_s^2 D \operatorname{sech}^2(y_s^2 D)}{\sqrt{\tanh(y_s^2 D)}} + \frac{L}{y_s^3} \right. \\ & \cdot \left\{ \sqrt{\tanh(K'_s D)} + \frac{K'_s{}^2 D \operatorname{sech}^2(K'_s D)}{\sqrt{\tanh(K'_s D)}} (y_s^3 + y_s \cos \theta_s \right. \\ & \left. \left. + D y_s^3 \operatorname{sech}^2(y_s^2 D) \sin \theta_s \frac{\cos(\theta_s + \beta)}{\sin(\theta_s + \beta)} \right) \right] \end{aligned} \quad (70)$$

The integration in (66) is performed using the numerical methods described in the preceding section. First it is reduced to a single dimensional integral by solving the delta function constraint. Frequency contours are defined by

$$\eta - h(y_s^*, \theta) = 0 \quad (71)$$

Due to wave refraction, the shallow water angle θ_s and the value of K_s at a given Doppler frequency have discontinuities when the incidence angle of the deep water wave at the depth contour is 0° or 180° , i.e., from Figure 8 when

$$\theta = -\beta, \pi - \beta \quad (72)$$

Examples of frequency contours in the (p, q) plane given in Figure 9 show gaps due to these discontinuities. Similarly, a gap occurs in the singular contour of the electromagnetic coupling coefficient defined by

$$\vec{K}_s \cdot \vec{K}'_s = 0 \quad (73)$$

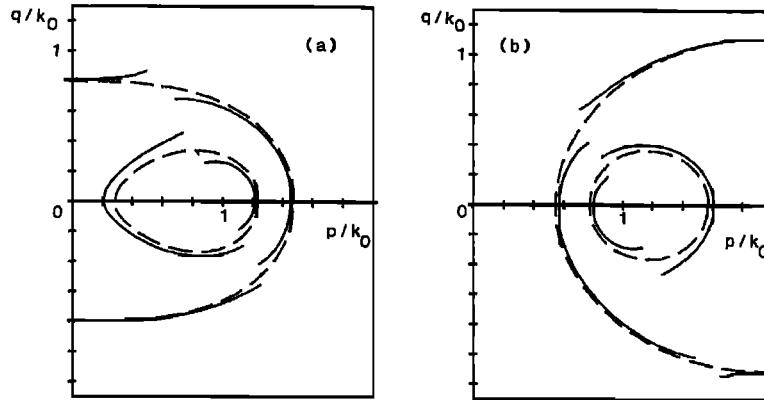


Fig. 9. Examples of frequency contours for water of depth 5 m. (continuous line) compared with the corresponding contours for deep water (dashed line). Angle between the radar beam and depth contour is 60°. Normalized frequency: (a) 1.4 (inner curve), 1.6 (outer); (b) 0.6 (inner), 0.4 (outer). Contours are symmetric about the q axis.

which from (65) is equivalent to

$$K_s = -\cos \theta_s \quad (74)$$

An example of the singular contour is given in Figure 10.

Simulated shallow water radar spectra are shown in Figure 11. The energy in the second-order spectrum increases as the water depth decreases. This effect becomes apparent close to the Bragg line, where the second-order spectrum arises from interactions between the radar wave and the longest ocean waves. These are steepened due to second-order nonlinearities, as manifested by the increasing value of the coupling coefficient as the water depth decreases. Similar increases in the second-order Doppler peaks

with decreasing water depth occur for any radar/wave angle.

2.3. The effect of ocean surface currents

When an incident radar wave \vec{k}_i interacts with an ocean wavetrain that is transported by a current of velocity \vec{v} to produce a scattered wave \vec{k}_s , the Doppler shift imposed is given by

$$\delta\omega = -\vec{k}_i \cdot \vec{v} + \vec{k}_s \cdot \vec{v} \quad (75)$$

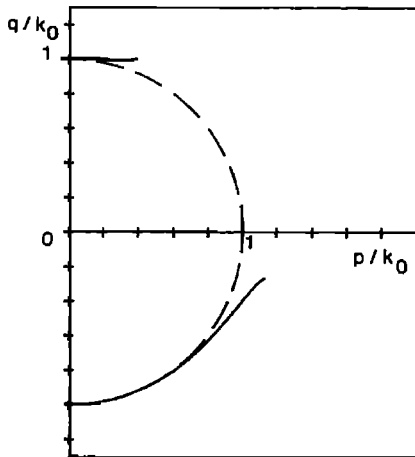


Fig. 10. The singular contour $K_s \cdot K'_s = 0$ of the electromagnetic coupling coefficient (continuous line) for water of depth 5 m. compared with that for deep water (dashed).

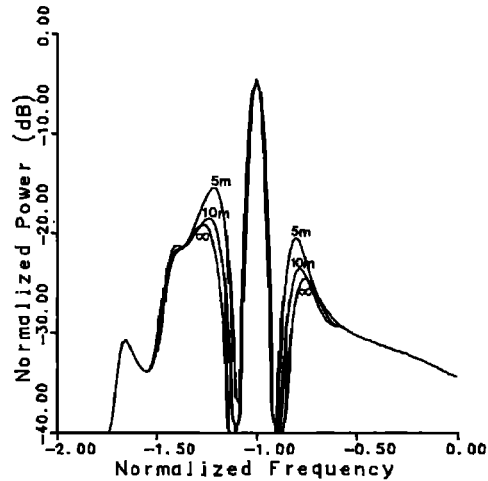


Fig. 11. Simulated spectra showing the effect of decreasing water depth. The ocean wave spectral model and frequency smearing are the same as for Figure 5; normalized cutoff wavenumber 0.1, dominant ocean-wave direction 45° with respect to the radar beam, which is perpendicular to the depth contour. The second-order peak increases as the depth decreases, the three curves corresponding to water depths of 5 m., 10 m. and infinite depth.

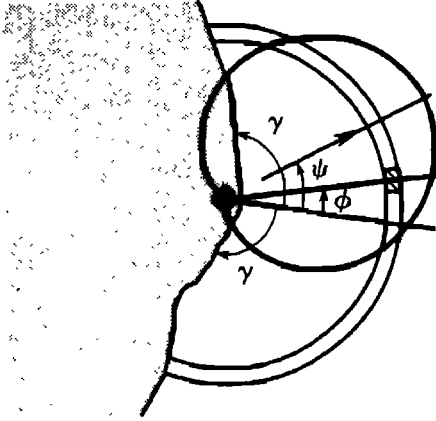


Fig. 12. Sketch of the CODAR beam pattern showing a circular range ring. The scan angle ψ , the coastline angle γ and a general angle ϕ are defined with respect to the bisector of the partial ring of sea.

For the first-order scatter by a Bragg ocean wave this becomes

$$\delta\omega^{(1)} = -2\vec{k}_0 \cdot \vec{v} \quad (76)$$

whereas for the second-order interaction illustrated in Figure 2, the total Doppler shift is the sum of the contributions from the two separate interactions:

$$\delta\omega^{(2)} = -\vec{k}_0 \cdot \vec{v} + \vec{k} \cdot \vec{v}' - \vec{k} \cdot \vec{v}'' - \vec{k}_0 \cdot \vec{v} \quad (77)$$

where the wavetrains are transported with velocities \vec{v} and \vec{v}' .

For a constant surface velocity, \vec{v} is equal to \vec{v}' and thus the whole spectrum is shifted uniformly by an amount proportional to the current velocity. As the first-order peak frequency in the absence of currents is known (2), such shifts are readily identified and removed from the data.

We now examine the effect of current gradients on the narrow-beam radar sea-echo. Vincent [1979] and Peregrine [1976] show that the wave dispersion equation is unaffected by horizontal variations of current with respect to the moving parcel of water at a given point. Therefore, since the cell area of a narrow-beam radar is nearly always small compared to the scale of horizontal current variations, we can ignore their effect on narrow-beam radar spectra. Vertical current shear produces a small frequency dependent shift over the Doppler spectrum since the phase speeds of long and short waves are affected in different measure; it is shown in Appendix B that this frequency differential is negligible in practice.

3. CODAR SEA ECHO

Lipa and Barrick [1983] give a detailed description of the CODAR system and its application to ocean current measurement. CODAR electronically forms and scans a broad beam over a circular range cell. In this section, we describe how CODAR's output is represented in terms of the directional ocean wave spectrum and ocean surface current and discuss the effects of inhomogeneous ocean conditions over the scattering region.

The CODAR system presently in use has a composite receiving antenna consisting of two crossed loops and a monopole. Lipa and Barrick [1983] describe how the voltage time series from the separate elements are Fourier transformed to give complex voltage spectra. The averaged voltage cross spectra are combined to effect the rotation of a broad beam (with a $\cos^4(\theta/2)$ pattern with respect to the beam maximum). The experimental situation is demonstrated in Figure 12. The broad beam return at a scan angle ψ is the convolution of the narrow beam radar cross section and the antenna pattern:

$$\bar{\sigma}(\omega, \psi) = \frac{1}{2\gamma} \int_{-\gamma}^{\gamma} \cos^4\left(\frac{\psi - \phi}{2}\right) \sigma(\omega, \phi) d\phi \quad (78)$$

where the angle subtended by the coastline at the radar is 2γ . The right hand side of (78) may be expressed as a Fourier series with exactly five nonzero coefficients:

$$\bar{\sigma}(\omega, \psi) = \frac{1}{2\pi} \sum_{n=-2}^2 b_n(\omega) t_f^n(\psi) \quad (79)$$

where the trigonometric functions are defined in (23). Lipa and Barrick [1983] show how the Fourier coefficients $b_n(\omega)$ are expressed in terms of the raw data and derive their relationship to the narrow-beam radar cross section:

$$b_n(\omega) = q_n \frac{\pi}{\gamma} \int_{-\gamma}^{\gamma} \sigma(\omega, \phi) t_f^n(\phi) d\phi \quad (80)$$

where $q_{-2} = q_2 = 1/8$; $q_{-1} = q_1 = 1/2$; $q_0 = 3/8$. The five Fourier coefficients may be regarded as convenient intermediate data products; note that if a narrow beam (i.e., an angular impulse function) could be rotated in a similar fashion, an infinite number of Fourier coefficients could be produced.

We define the following dimensionless form for the Fourier coefficients in the first and second order regions:

$$B_n^{1,2}(\eta) \equiv \frac{\omega_B b_n(\omega)\gamma}{q_n \pi} = \int_{-\gamma}^{\gamma} \sigma_{1,2}(\eta, \phi) t_f^n(\phi) d\phi \quad (81)$$

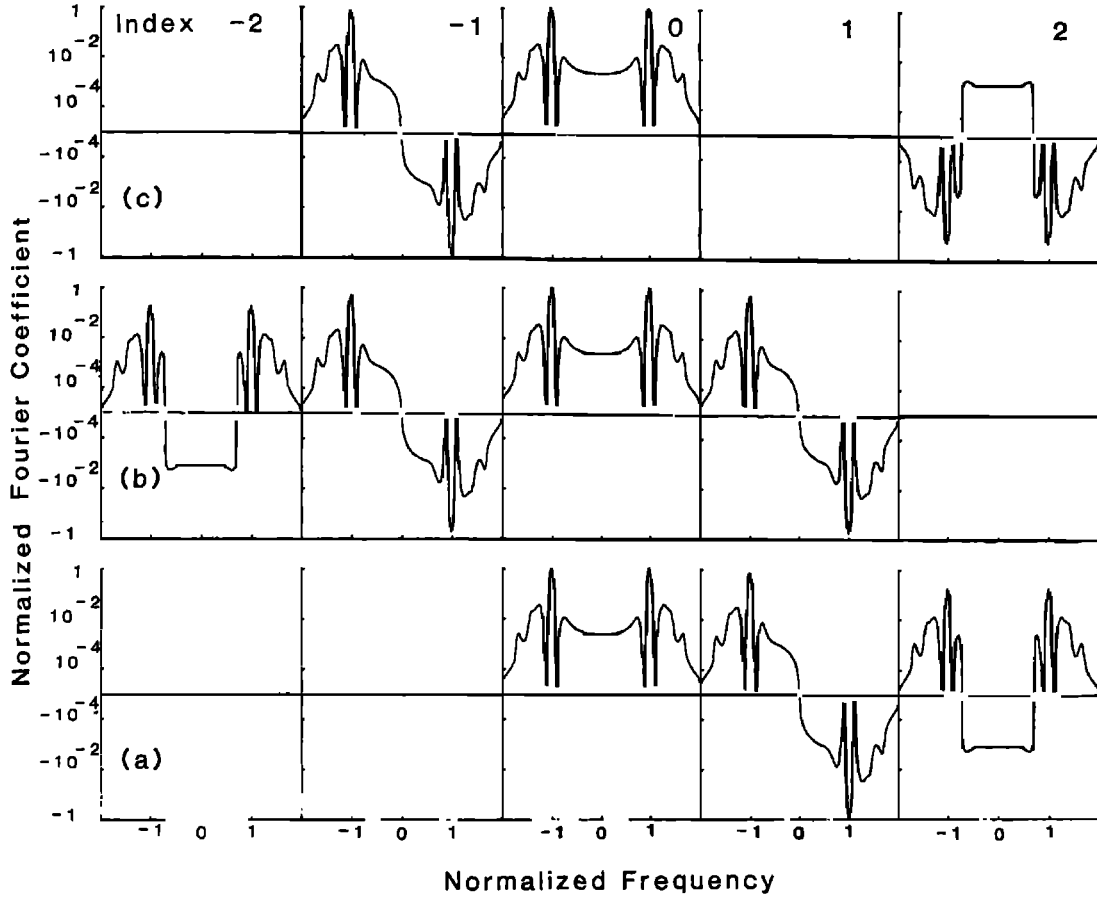


Fig. 13. Simulated radar Fourier coefficient spectra for deep water platform operation. The ocean-wave spectral model and frequency resolution used are the same as for Figure 5; normalized cutoff wavenumber 0.1; ocean-wave direction (a) 90°, (b) 45°, (c) 0°. The upper/lower half of each figure represents positive/negative spectral values, plotted on a logarithmic scale.

where $\sigma_{1,2}(\eta, \phi)$ are the normalized narrow beam radar cross sections defined by (41) and (42) for deep water, or by (63) and (64) for shallow water. In general, the integration over azimuth angle must be performed numerically; we have used a simple trapezoidal rule with an angular increment of 10°.

3.1. Homogeneous ocean wave spectrum

If the water depth and the ocean wave spectrum are homogeneous over the entire range cell, the narrow-beam radar cross section has the same functional form at each azimuth angle. As an example, we have simulated results for the ocean spectral model described in section 2 and deep water completely surrounding the radar (i.e., $\gamma = 180^\circ$). This simulation is appropriate to operation from a deep-water platform at close range. The radar Fourier coefficients $B_n^{1,2}(\eta)$

are then symmetric/antisymmetric functions of frequency for even/odd values of n . This follows from (81), since for homogeneous conditions the advancing, positively shifted sea echo at azimuth angle ϕ has the same magnitude as the receding, negatively shifted echo directly on the other side of the radar, i.e.,

$$\sigma_{1,2}(\eta, \phi) = \sigma_{1,2}(-\eta, \phi + \pi) \quad (82)$$

Substitution of (82) into (81) gives

$$B_n^{1,2}(\eta) = (-1)^n B_n^{1,2}(-\eta) \quad (83)$$

In this case, closed form solutions exist for the first-order sea-echo. Substitution of (41) into (81) gives

$$B_n^2(\eta) = 4\pi \sum_{m=\pm 1} \delta(\eta - m') \int_{-\pi}^{\pi} Z(-m'k_0) f_n(\phi) d\phi \quad (84)$$

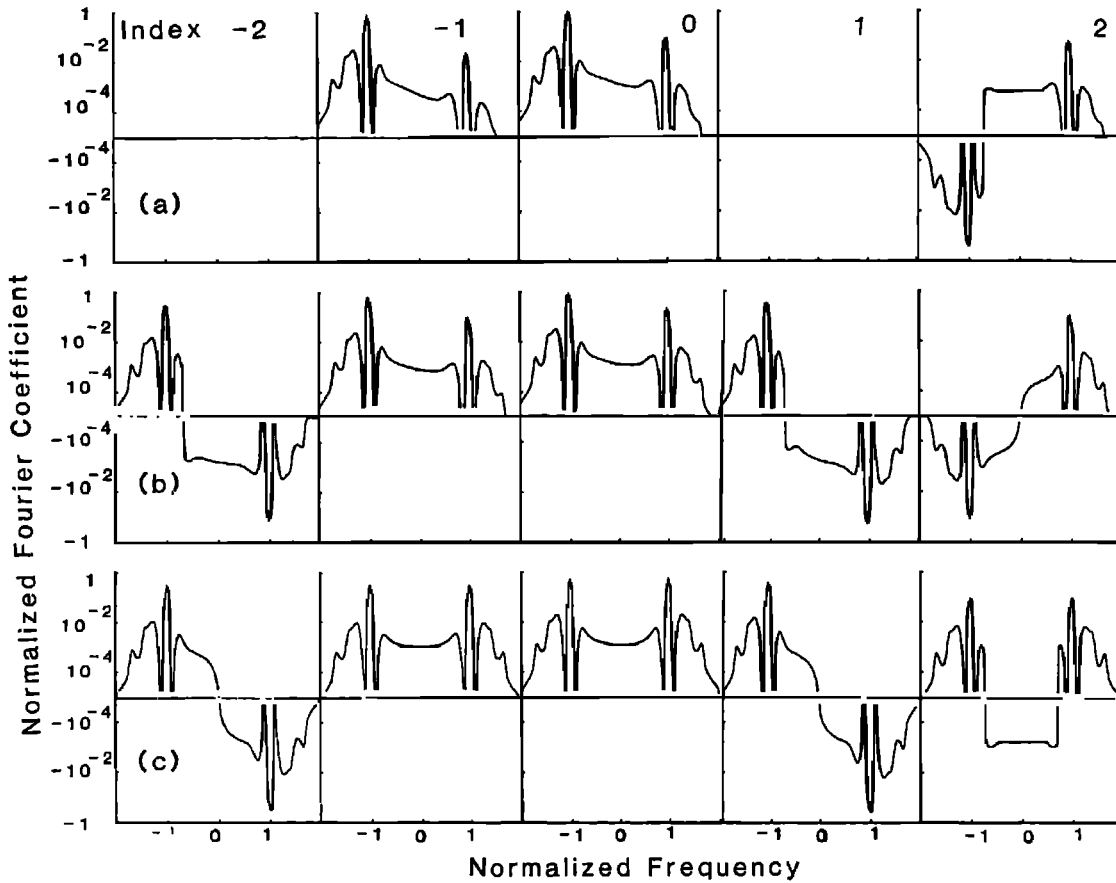


Fig. 14. As for Figure 13, but for operation from a straight coastline.

where from (20), (21), (22), and (33)

$$Z(-m'k_0) = \frac{0.005e^{-0.37K_c}}{2\pi} \sum_{n=-2}^2 c_n t_n \left(\phi + \left[\frac{m'+1}{2} \right] \pi \right) \quad (85)$$

Integration over azimuth angle gives

$$B_n^1(\eta) = 0.02\pi e^{-0.37K_c} c_n \sum_{m'=\pm 1} \delta(\eta - m'(-1)^{(m'+1/2)n}) \quad (86)$$

i.e., the radar Fourier coefficients are directly proportional to the ocean wave spectral Fourier coefficients. The second-order results must be obtained by numerical integration. Results are given in Figure 13.

When the radar operates from a straight coastline ($\gamma = 90^\circ$), the frequency symmetry (83) no longer holds; thus the CODAR output contains more information on the directional spectrum when it operates from shore. Figure 14 gives the simulated radar Fourier coefficients for this case.

3.2. Inhomogeneous ocean wave spectrum

If the directional spectrum varies around the range cell, the functional form for the narrow-beam radar cross section in (81) is different at each azimuth. This would apply, for example, to operation from a platform at distant ranges where the range cell extends over a wide area of ocean. In this case the spectral symmetry described by (83) would no longer be expected to hold.

As another example of inhomogeneous conditions, we consider operation from a coast where the range cell extends over water of varying depth (Figure 15). In this case, the range cell is divided into N segments by its intersection with selected depth contours. In the j th segment, bounded by azimuth angles ϕ_j and ϕ_{j+1} , we define an average angle between the radar beam and constant-depth contour (β_j) and an average depth D_j . The radar coefficients are then defined by

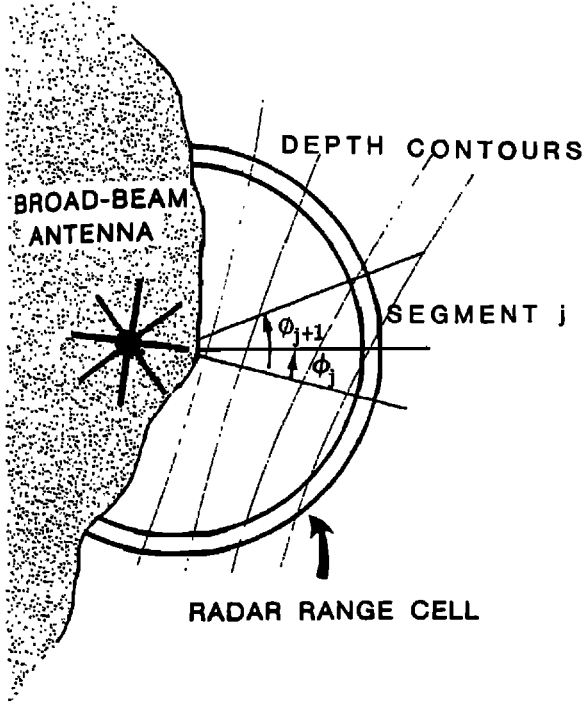


Fig. 15. Schematic diagram of CODAR operation from a coast over shallow water of varying depth, showing the division of the range cell into segments by constant depth contours.

$$B_n^{1,2}(\eta) = \sum_{j=1}^N \int_{\phi_j}^{\phi_{j+1}} \sigma_{1,2}^2(\eta, \phi, D_j, \beta_j) t f_n(\phi) d\phi \quad (87)$$

where Figure 15 shows that by symmetry

$$D_j = D_{N-j+1} \quad (88)$$

At the normal CODAR operating frequency of 25.4 MHz, the water depth must be less than 2 m to affect the 2-s first-order Bragg-scattering waves significantly. Hence the problem is simplified by the fact that the first-order Doppler spectrum is always effectively the deep-water result; shallow water need be considered only for the second-order return produced by the longer ocean waves that are first affected by decreasing water depth.

3.3. Effect of ocean surface currents

3.3.1. *Uniform current.* For a narrow-beam radar, a current velocity in the scattering region causes the whole spectrum to be displaced by an amount proportional to the current velocity, defined in (76). However the extended CODAR range cell has a different value of radial current velocity at each azimuth angle, resulting in frequency smearing in the

spectrum. For a current velocity pattern defined by radial components $v_{cr}(\phi)$, (80) becomes

$$b_n(\omega) = \frac{q_n \pi}{\gamma} \int_{-\gamma}^{\gamma} \sigma(\omega - 2k_0 v_{cr}(\phi), \phi) t f_n(\phi) d\phi \quad (89)$$

We define a normalized velocity $V(\phi)$ such that

$$V(\phi) = v_{cr}(\phi)/v_{ph} \quad (90)$$

where v_{ph} is the phase velocity of the first-order Bragg-scattering wave trains, which is given in terms of the radar wavenumber for deep water by

$$v_{ph} = \sqrt{\frac{g}{2k_0}} \quad (91)$$

In normalized form, (89) becomes

$$B_n^{1,2}(\eta) = \int_{-\gamma}^{\gamma} \sigma_{1,2}(\eta - V(\phi), \phi) t f_n(\phi) d\phi \quad (92)$$

Inserting (41) into (92) gives for the first-order region:

$$B_n^1(\eta) = 4\pi \sum_{m'=\pm 1} \int_{-\gamma}^{\gamma} Z(-mk_0) \delta(\eta - m' - V(\phi)) t f_n(\phi) d\phi \quad (93)$$

Therefore the first-order peak is not only displaced in frequency (as it is for a narrow beam) but is also broadened into a form that depends on the current velocity pattern. It is by interpretation of the radar data in terms of (93) that the current velocity map is derived [Lipa and Barrick, 1983]. Similarly, the second-order spectrum in the presence of current smearing is obtained by substituting (42) into (92).

Simulated results for a uniform current flowing past a platform are shown in Figure 16, for the spectral model described in section 2. A uniform current of speed V_c and angle ϕ_c has a velocity pattern described by

$$V(\phi) = V_c \cos(\phi - \phi_c) \quad (94)$$

Substituting (85) and (94) into (93) gives a closed form solution in the first-order region:

$$B_n^1(\eta) = 0.01 \sum_{m'=\pm 1} \sum_{j=-2}^2 c_j t f_j \left[\phi^* + \left(\frac{m'+1}{2} \right) \pi \right] \begin{cases} |\eta - m'| \leq V_c \\ = 0 \\ |\eta - m'| > V_c \end{cases} \quad (95)$$

where the angle ϕ^* is defined by the delta function constraint to be

$$\phi^* = \phi_c + \cos^{-1} \left(\frac{\eta - m'}{V_c} \right) \quad (96)$$

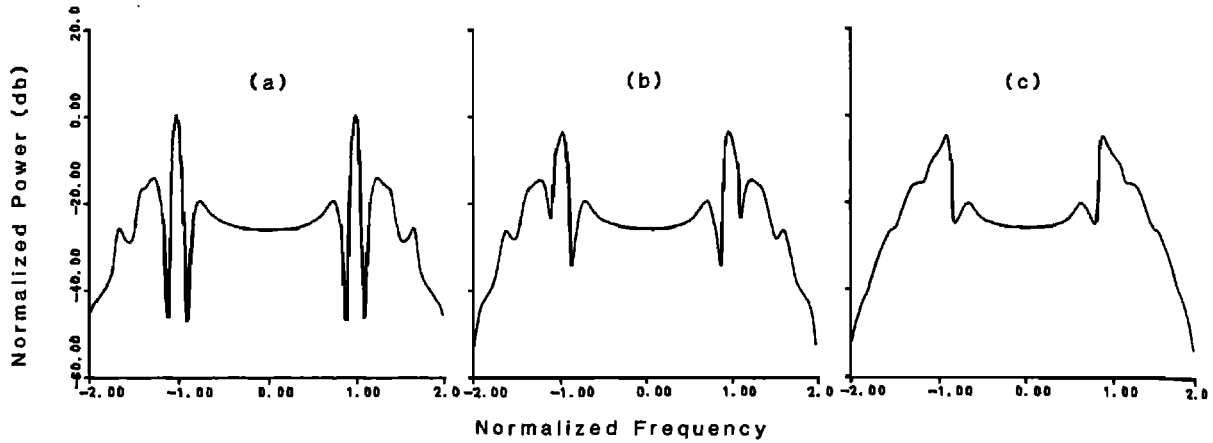


Fig. 16. The nondirectional Fourier spectral coefficient for increasing current velocity, deep-water platform operation, with the ocean-wave spectral model and frequency smearing as for Figure 13. Normalized current velocity: (a) 0, (b) 0.66, (c) 0.132. This is equivalent to a radar transmitter frequency of 25.4 MHz and current velocities of (a) zero, (b) 20 cm/s, (c) 40 cm/s.

Thus the first-order region which in the absence of surface current is an impulse function is now spread over a region with normalized frequency width $2V_c$. The second order spectrum must be obtained by numerical integration. It is easy to show that for a uniform current (for which $V(\phi) = -V(\phi + \pi)$ the symmetry property (83) still holds. This follows from (84) by noting that for a homogeneous directional spectrum

$$\begin{aligned} \sigma_{1,2}[-\eta - V(\phi), \pi] &= \sigma_{1,2}(\eta + V(\phi), \phi + \pi) \\ &= \sigma_{1,2}(\eta - V(\phi + \pi), \phi + \pi) \end{aligned} \quad (97)$$

The current smearing of the ideal spectrum evident in Figure 16 results in a loss of frequency resolution in the directional spectrum derived from CODAR output. For a strong current velocity, this effect can be reduced by use of a lower radar transmit frequency.

3.3.2. *Horizontally shearing current.* It is shown in Appendix B that the effects of typical vertical current shears on the radar spectrum are small. In section 1, we concluded that horizontal current gradients do not affect the narrow-beam Doppler spectrum significantly. This is not necessarily true for CODAR observations which are made over an extended range cell. For horizontal current variation along the direction of flow, both *Peregrine* [1976] and *Vincent* [1979] show that the greatest interaction occurs when the current is parallel to a wave-train. Although the phase velocity of the wave relative to a stationary observer is increased by the current velocity, the wave dispersion equation between

the spatial and temporal wavenumbers is unchanged. The wave amplitude and hence the wave spectrum varies with position on the current trajectory but this variation is insignificant for normal CODAR operation; for example analysis of *Peregrine's* equations for onshore tidal flow in typical coastal situations with water depths of ~ 20 m. shows that the variation in wave amplitude is less than 10% over distances of the order of 150 km and can therefore be ignored over a 30 km Codar range cell.

Current variations across the direction of flow cause refraction of waves with changes in direction, height, wavenumber and steepness. In *Peregrine's* detailed analysis, it is assumed that the scales of current variation are far greater than a wavelength, that both waves and currents are steady state, that there is no energy exchange between waves and currents and no energy dissipation. The wave dispersion equation is unaffected and wave refraction occurring on a horizontal shear obeys laws similar to those governing refraction in shallow water:

$$k_2 \cos \phi_2 = k_1 \cos \phi_1 \quad (98)$$

$$k_2 = k_1(1 - u^* \cos \phi_1)^2 \quad (99)$$

where ϕ_1 and ϕ_2 are the angles between the wavevector and current direction before and after refraction; k_1 and k_2 are the corresponding wavenumbers; u^* is the fractional change in current velocity u with respect to the initial wave phase velocity $c_1 = (g/k_1)^{1/2}$:

$$u^* = \Delta u / c_1 \quad (100)$$

TABLE 1. Reflection of 10-s Wave on 40 cm/s Velocity Shear, With Respect to the Initial Angle Between Wave and Current Directions (ϕ)

ϕ_1 , deg	$\phi_1 - \phi_2$, deg
0	reflection
10	reflection
20	-10.6
30	-4.9
40	-2.8
50	-1.6
60	-0.9
70	-0.4
80	-0.1
90	0.0

The amount of refraction decreases with wave frequency and with the angle between the current and the wave direction. Wave refraction in regions of large current shear such as the Gulf Stream can be extreme. These regions also have high current velocity with the corresponding smearing of the radar spectrum described previously; therefore CODAR cannot at present be used to measure waves in these regions and we restrict consideration to current shears of less than 40 cm/s. For a 10 s ocean wave refracting across this maximum shear, analysis of (98)–(99) indicates that the wavenumber changes by less than 2%; the direction change for a given incidence angle is given in Table 1. This shows that wave reflection is restricted to a cone of 12° about the current direction and the amount of wave refraction occurring outside this cone is less than 11° . Since these refraction effects are slight, we have not included equations (98)–(99) in the analysis, although this could be done in a similar way to the inclusion of the equations describing shallow water refraction.

4. CONCLUSION

In this paper, we have described analytical techniques for the modeling of HF radar sea-echo Doppler spectra, discussing their prominent features and their dependence on ocean conditions commonly encountered in experimental situations. Using wind-wave models of the ocean waveheight directional spectrum, four dominant peaks, two each surrounding the first-order Bragg peaks, are clearly evident in the modeled spectra for both narrow- and broad-beam radars. These second-order peaks arise from the interaction of the dominant ocean waves with the short, first-order Bragg-scattering waves (of 2-s period at 25 MHz radar frequency). Secondary

peaks occur at $2^{1/2}$ and $2^{3/4}$ times the Bragg Doppler frequency, resulting from integrable mathematical and electromagnetic singularities, respectively; these are due to the interaction of short waves, and hence contain little information on “sea-state” at normal HF frequencies. For both narrow- and broad-beam radars, increasing the wind speed driving the Pierson-Moskowitz ocean spectral model causes the second-order peaks to increase relative to the first-order; we show that the spectral shape at a given wind speed is dependent on the radar/dominant-wave direction. This sensitivity of the radar spectrum to both waveheight and direction indicates that its inversion will yield parameters of the waveheight directional spectrum.

We identify a limiting value of the ocean waveheight at which the perturbation solution for the radar sea-echo spectrum at a given transmit frequency becomes invalid due to spectral saturation; either a lower transmit frequency must then be used, or the theory extended to apply to the saturated spectrum.

Water that is shallow with respect to the dominant waves present is usually encountered in coastal measurement situations. The modeling of the shallow-water radar spectrum must account for the linear angular refraction and linear spatial wavenumber transformation that long ocean waves undergo when they pass from deep to shallow water. In addition, it must include the shallow-water hydrodynamic coupling coefficient that produces the second-order nonlinear waveheight directional spectrum, and hence the second-order radar Doppler spectrum. This causes the second-order Doppler peaks to increase relative to the first as the water depth decreases. Conversely, neglecting the effects of finite water depth for the long ocean waves can lead to waveheight estimates which are too low as well as incorrect long-wave directions.

Using the narrow-beam expressions for first- and second-order sea-echo in the formulation of the broad-beam return from a CODAR crossed-loop system gives five Fourier angular coefficients as a function of Doppler frequency. This is analogous to the five Fourier coefficients vs wave frequency obtained from pitch and roll wave buoys that measure the directional spectrum. The CODAR angular coefficients are shown to depend strongly on the dominant wave direction when CODAR is operated from an island or platform completely surrounded by water and the dependence is even stronger when CODAR operates from shore.

Finally, we describe the effects of ocean surface currents on the radar sea echo. Uniform currents produce different effects on narrow- and broad-beam Doppler spectra. In the former, they produce a frequency shift of the entire spectrum, which is easily identified and removed. In the latter, frequency smearing in the entire spectrum results which is representable as a convolution of the radial current pattern over azimuth angle with the zero-current spectrum. Strong currents in the broad-beam coverage area therefore decrease the frequency resolution in the Doppler spectrum and in the retrieved wave-height directional spectrum obtained by inversion. The inversion process must take account of current smearing, employing the knowledge of the current pattern derived from the first-order region to interpret the second-order spectrum.

We show that the radar spectrum is not significantly affected by vertical current shear. Horizontal current gradients leave the wave dispersion equation unchanged but cause wave refraction and inhomogeneity in the directional ocean wave spectrum over the extended range cells of a broad-beam radar system. We show how this effect can be modeled; it has not yet been included in the CODAR analysis, as at present we are restricting CODAR wave measurements to regions of moderate surface current velocity and velocity gradients where both the wave refraction and the loss of frequency resolution are unimportant.

This paper identifies ocean surface parameters to which the radar sea-echo Doppler spectrum is sensitive, and establishes the degree of sensitivity of dominant spectral features. This step is required before the development of inversion methods for the extraction of sea-state information from the second-order spectrum, which will be described in a subsequent paper. These inversion methods, based on maximum likelihood, minimize the variance between the data and the radar spectral models described here.

APPENDIX A: THE COUPLING COEFFICIENTS

The hydrodynamic coupling coefficient, Eq. (7), has been derived by *Weber and Barrick [1977]*, and physically represents the generation of a second-order ocean wave that produces first-order radar backscatter by the Bragg mechanism; formed by the nonlinear hydrodynamic boundary conditions at the surface, the wave is "bound" to the two first-order waves that produce it. In this appendix we (i) show how the electromagnetic coupling coefficient presented by *Barrick [1972b]* is obtained explicitly from

Rice's [1951] original work, and (ii) correct and explain the meaning of an important term we add that avoids a non-integrable singularity in the latter.

Rice represents the randomly rough, perfectly conducting surface and the electromagnetic field above it as two-dimensional Fourier series. The electromagnetic boundary condition at the surface is expanded as a perturbational ordering in surface slopes and surface height relative to radar wavelength (both small for the sea at HF and lower). To second order the solution for scatter for a vertically polarized incident wave is given by his Eq. (4.2); the second summation over k, l of E_z of this equation contains the desired coupling coefficient for vertically polarized scatter. It is reduced to the form given in (8) above by (1) noting in Rice's expression that for backscatter at grazing incidence $av = k_0 \sin \theta_i \rightarrow +k_0$; $am = k_0 \sin \theta_s \cos \varphi_s \rightarrow -k_0$; $an = k_0 \sin \theta_s \sin \varphi_s \rightarrow 0$ (where θ_i is the incidence angle from vertical and θ_s, φ_s are the polar and azimuthal scatter angles with respect to the incidence plane); (2) substituting wavenumbers $ak \rightarrow p$ and $al \rightarrow q$ in order to change from Rice's series to our integral representations of (3); (3) making the coupling coefficient symmetrical in \mathbf{k} and \mathbf{k}' (the latter ocean wavenumbers are defined in (4) in terms of p, q), i.e., by using (5) and replacing terms like $f(\mathbf{k})$ by their symmetrical equivalent $[f(\mathbf{k}) + f(\mathbf{k}')]/2$. (The latter two steps are not necessary for correctness, but only for mathematical convenience in subsequent evaluation of integrals, allowing use of symmetry to reduce numerical computations.) Finally, the extension from Rice's modal series solutions valid for random periodic surfaces of infinite extent to random large, but finite, scattering patches is done by applying either geometrical arguments or Kirchhoff-type transformations, both used and discussed in *Barrick [1972a]*, *Barrick [1970]*, and *Peake [1959]*.

The coupling coefficient obtained in the above manner from Rice is identical to (8) above, except there is no term $-k_0 \Delta$ in the denominator, only $(\mathbf{k} \cdot \mathbf{k}')^{1/2}$. The latter can be written as κ_{iz} , with $\tilde{\mathbf{k}}_i = (p, q)$, where Eqs. (4) and (5) lead to the physical interpretation of $\tilde{\mathbf{k}}_i$ as the intermediate wavevector of the field scattered (either propagating or evanescent) between ocean waves with wavevectors $\tilde{\mathbf{k}}$ and $\tilde{\mathbf{k}}'$. (The presence of $\kappa_{iz} = (\tilde{\mathbf{k}} \cdot \tilde{\mathbf{k}}')^{1/2}$ in the denominator can also be established independently by considering the combination of two first-order scattering processes for vertical polarization at grazing incidence [*Barrick, 1972a*].) When κ_{iz} vanishes, this means the intermediate wave is propagating directly parallel to,

and is polarized completely perpendicular to the mean surface; large energy is then transferred in the double-interaction process. This happens when the two scattering ocean waves are perpendicular to each other, i.e., $\vec{k} \cdot \vec{k}' = 0$, commonly referred to as the "corner-reflector" condition [Lipa and Barrick, 1980]. Left as the only term in the denominator of (8), the condition $\vec{k} \cdot \vec{k}' \rightarrow 0$ in the integration of (3) produces a non-integrable singularity.

However, it is impossible for a vertically polarized wave to propagate exactly parallel to any surface that is imperfect, and satisfy the required boundary conditions at the interface. Both roughness and finite conductivity of the medium below the surface force an effective boundary condition at the mean interface that gives an apparent vertical wavevector component $\kappa_{iz} \rightarrow -k_0 \Delta$ (even when $(\vec{k} \cdot \vec{k}')^{1/2}$ vanishes) directed into the surface [Barrick, 1971; Bahar, 1982], with Δ being the average, normalized impedance at the interface. This justifies the addition of $-k_0 \Delta$ to the denominator, as it appears in (8), and corrects a sign error preceding this term in Barrick [1972b]. (The sign reversal actually causes negligible error in the integration.) Barrick [1971] has shown that for the rough, imperfect sea at HF, a reasonable impedance is $\Delta = 0.011 - 0.012$ at 10 MHz; the effect of its slight variation across the HF band is significantly minimal in the integration of (3) that it can be considered a constant.

APPENDIX B: EFFECT OF VERTICAL CURRENT SHEAR ON THE NARROW-BEAM DOPPLER SPECTRUM

In the text, it has been shown that a current that is constant both laterally and vertically across the scattering patch produces a uniform frequency shift across the entire Doppler spectrum. In this appendix, we examine the differential frequency shifts produced by a vertical current shear and show these effects to be negligible in realistic situations.

Both Stewart and Joy [1974] and Ha [1979] have shown that the apparent phase velocity of a wave-train with wavevector $\vec{\zeta}$, frequency χ and phase speed c is increased in the presence of a vertical current shear $\vec{v}(z)$ by the amount

$$\Delta c = \zeta \int_0^{\infty} 2\vec{\zeta} \cdot \vec{v}(z) e^{-2|\zeta|z} dz \quad (\text{B1})$$

where z is depth measured downwards from the mean surface. This is the perturbation solution to an Orr-Sommerfeld differential equation to first order in

the parameter $|\zeta|a$ where a is the wave amplitude. This solution for infinite depth is obtained with the following assumptions, which are shown to be generally applicable:

$$\begin{aligned} |\zeta|a < 1 & \quad |\vec{v}(z)|/c < 1 \\ \frac{|dv(z)/dz|_{z=0}}{\chi} < 1 & \quad \frac{|d^2v(z)/dz^2|_{z=0}}{|\zeta|\chi} < 1 \end{aligned} \quad (\text{B2})$$

Applying equation (B1) to equations (2) and (10) or (15) for the first and second order Doppler shift due to current gives

$$\delta\omega^{(1)} = -4k_0 \int_0^{\infty} 2\vec{k}_0 \cdot \vec{v}(z) e^{-4k_0 z} dz \quad (\text{B3})$$

$$\delta\omega^{(2)} = 2k \int_0^{\infty} \vec{k} \cdot \vec{v}(z) e^{-2kz} dz + 2k' \int_0^{\infty} \vec{k}' \cdot v(z) e^{-2k'z} dz \quad (\text{B4})$$

where \vec{k} and \vec{k}' are the wavevectors of the ocean waves producing the second-order scatter, and \vec{k}_0 is the radar wavevector.

Both theory and measurement show that the current is a maximum at the surface and decreases with depth to a constant value. Since we showed in the text that a constant term does not produce differential frequency shifts, we consider here only an exponential depth variation, decaying to zero at an infinite depth

$$\vec{v}(z) = \vec{v}_0 e^{-\gamma z} \quad (\text{B5})$$

This form is predicted for a Stokes drift [Kinsman, 1965] and is shown by Ha [1979] to be a good approximation near the surface. He finds that for ~ 12 knot wind conditions with $|v_0| = 15$ cm/s, the parameter γ is approximately 0.35 m^{-1} . Substituting (B5) into (B3) and (B4), we obtain the following expression for the difference between the first and second order current shifts:

$$\begin{aligned} \delta\omega^{(2)} - \delta\omega^{(1)} &= \frac{k}{k + \gamma} \vec{k} \cdot \vec{v}_0 + \frac{k'}{k' + \gamma} \vec{k}' \cdot \vec{v}_0 \\ &\quad - \frac{2k_0}{2k_0 + \gamma} (-2\vec{k}_0 \cdot \vec{v}_0) \end{aligned} \quad (\text{B6})$$

This expression can be seen to tend to zero as $\gamma \rightarrow 0$ (i.e., no vertical variation), since $\vec{k} + \vec{k}' = -2\vec{k}_0$. It also becomes zero at the Bragg frequency, as $\vec{k} \rightarrow 0$ and $\vec{k}' \rightarrow -2\vec{k}_0$; physically this means that the shear is not felt by the infinitely long wave.

The value of the Doppler differential is directly proportional to the current speed and has its maxi-

TABLE B1. The Bounds on the Doppler Frequency Differential for Typical Vertical Current Shear

Normalized Doppler Shift From Bragg Frequency (Equation (34))	Doppler Frequency Differential, Hz	
	Maximum	Minimum
-0.97	0.0051	-0.0084
-0.83	0.0049	-0.0083
-0.69	0.0044	-0.0080
-0.55	0.0037	-0.0069
-0.41	0.0028	-0.0049
-0.28	0.0016	-0.0025
-0.14	0.0005	-0.0007
0.	0.	0.
0.14	0.0007	-0.0005
0.28	0.0026	-0.0016
0.41	0.0051	-0.0028
0.55	0.0036	-0.0039
0.69	0.0023	-0.0048
0.83	0.0012	-0.0055
0.97	0.0002	-0.0061

imum magnitude when the current is directed along the radar beam. Calculations of the Doppler differential around the frequency contour at each spectral point show that it is small over the important region of the Doppler spectrum; hence the remaining constant current shift common to both first- and second-order sea-echo is easily removed as before. Results are given in Table B1 for $\gamma = 0.35 \text{ m}^{-1}$, $|v_0| = 20 \text{ cm/s}$ and the CODAR transmit frequency of 25.4 MHz. The Doppler differential is of the same order or less than the CODAR frequency resolution (0.00745 Hz) over the entire Doppler spectrum.

REFERENCES

- Bahar, E., Scattering and depolarization of electromagnetic waves near grazing angles, *IEEE Trans. Antennas Propag.*, AP-30, 712-719, 1982.
- Barrick, D. E., The interaction of HF/VHF radio waves with the sea surface and its implications, *Electromagnetics of the Sea, AGARD Conf. Proc.*, 77, 18.1-18.25, 1970.
- Barrick, D. E., Theory of HF and VHF propagation across the rough sea, 1, The effective surface impedance for a slightly rough highly conducting medium at grazing incidence, *Radio Sci.*, 6, 517-526, 1971.
- Barrick, D. E., First-order theory and analysis of MF/HF/VHF scatter from the sea, *IEEE Trans. Antennas Propag.*, AP-20, 2-10, 1972a.
- Barrick, D. E., Remote sensing of sea state by radar, in *Remote Sensing of the Troposphere*, edited by V. E. Derr, pp. 12-1-12-46, NOAA/Environmental Research Laboratories, Boulder, Colo., 1972b. (Available from U.S. Government Printing Office, Washington, D. C.)
- Barrick, D. E., and B. J. Lipa, A compact transportable HF radar system for directional coastal wave field measurements, in *Ocean Wave Climate*, edited by M. D. Earle and A. Malahoff, pp. 153-201, Plenum, New York, 1979.
- Barrick, D. E., and B. J. Lipa, The second-order shallow-water hydrodynamic coupling coefficient in interpretation of HF radar sea echo, *IEEE J. Oceanic Eng.*, OE-11, in press, 1986.
- Barrick, D. E., and J. A. Snider, The statistics of HF sea-echo Doppler spectra, *IEEE Trans. Antennas Propag.*, AP-25, 19-28, 1977.
- Barrick, D. E., and C. T. Swift, The Seasat instruments in historical perspective, *IEEE J. Oceanic Eng.*, OE-5, 74-79, 1980.
- Barrick, D. E., M. W. Evans, and B. L. Weber, Ocean surface currents mapped by radar, *Science*, 198, 138-144, 1977.
- Crombie, D. D., Doppler spectrum of sea echo at 13.56 Mc/s, *Nature*, 175, 681-682, 1955.
- Ha, E. C., Remote sensing of ocean surface current and current shear by HF backscatter radar, *Tech. Rep. D415-1 (SEL-79-022)*, Radiosci. Lab., Stanford Electron. Lab., Stanford, Calif., August 1979.
- Kinsman, B., *Wind Waves*, chap. 7.5, 676 pp., Prentice-Hall, New York, 1965.
- Lipa, B. J., and D. E. Barrick, Methods for the extraction of long-period ocean wave parameters from narrow-beam HF radar sea echo, *Radio Sci.*, 15, 843-853, 1980.
- Lipa, B. J., and D. E. Barrick, Analysis methods for narrow-beam high-frequency radar sea echo, *Tech. Rep. ERL 420-WPL 56*, NOAA, Boulder, Colo., 1982a.
- Lipa, B. J., and D. E. Barrick, CODAR measurements of ocean surface parameters at ARSLOE—Preliminary results, *Conf. Rec. IEEE Oceans 82*, 0197-7385/82, 901-906, 1982b.
- Lipa, B. J., and D. E. Barrick, Least-squares methods for the extraction of surface currents from CODAR crossed-loop data, *IEEE J. Oceanic Eng.*, OE-8, 226-253, 1983.
- Lipa, B. J., D. E. Barrick, and J. W. Maresca, Jr., HF radar measurements of long ocean waves, *J. Geophys. Res.*, 86, 4089-4102, 1981.
- Moskowitz, L., Estimates of the power spectrums of fully developed seas for wind speeds of 20 to 40 knots, *J. Geophys. Res.*, 69, 5161-5179, 1964.
- Peake, W. H., Theory of radar return from terrain, *IEEE Int. Conv. Rec.*, 7(1), 27-41, 1959.
- Peregrine, D. H., Interactions of water waves and currents, in *Advances in Applied Mechanics*, edited by C. S. Yih, pp. 9-117, Academic, Orlando, Fla., 1976.
- Rice, S. O., *Reflection of electromagnetic waves*, edited by M. Kline, pp. 351-378, Interscience, New York, 1951.
- Stewart, R. H., and J. W. Joy, HF radio measurement of surface currents, *Deep Sea Res.*, 21, 1039-1049, 1974.
- Vincent, C. E., The interaction of wind-generated sea waves with tidal currents, *J. Phys. Oceanogr.*, 9, 748-755, 1979.
- Weber, B. L., and D. E. Barrick, On the nonlinear theory for gravity waves on the ocean's surface, 1, Derivations, *J. Phys. Oceanogr.*, 7, 3-10, 1977.
- D. E. Barrick, Ocean Surface Research, 1131 Cranbrook Ct., Boulder, CO 80303.
- B. J. Lipa, Ocean Surface Research, 165 Harcross Rd., Woodside, CA 94062.